Draft version April 18, 2011
Preprint typeset using LaTeX style emulateapj v. 08/13/06

THE CENTRAL SLOPE OF DARK MATTER CORES IN DWARF GALAXIES: SIMULATIONS VS. THINGS

Se-Heon Oh[1,8], Chris Brook[2], Fabio Governato[3], Elias Brinks[4], Lucio Mayer[5], W.J.G. de Blok[1], Alyson Brooks[6] and Fabian Walter[7]

Draft version April 18, 2011

ABSTRACT

We make a direct comparison of the derived dark matter (DM) distributions between hydrodynamical simulations of dwarf galaxies assuming a ΛCDM cosmology and the observed dwarf galaxies sample from the THINGS survey in terms of (1) the rotation curve shape and (2) the logarithmic inner density slope α of mass density profiles. The simulations, which include the effect of baryonic feedback processes, such as gas cooling, star formation, cosmic UV background heating and most importantly physically motivated gas outflows driven by supernovae (SNe), form bulgeless galaxies with DM cores. We show that the stellar and baryonic mass is similar to that inferred from photometric and kinematic methods for galaxies of similar circular velocity. Analyzing the simulations in exactly the same way as the observational sample allows us to address directly the so-called "cusp/core" problem in the ΛCDM model. We show that the rotation curves of the simulated dwarf galaxies rise less steeply than CDM rotation curves and are consistent with those of the THINGS dwarf galaxies. The mean value of the logarithmic inner density slopes α of the simulated galaxies' dark matter density profiles is $\sim -0.4 \pm 0.1$, which shows good agreement with $\alpha = -0.29 \pm 0.07$ of the THINGS dwarf galaxies. The effect of non-circular motions is not significant enough to affect the results. This confirms that the baryonic feedback processes included in the simulations are efficiently able to make the initial cusps with $\alpha \sim -1.0$ to -1.5 predicted by dark-matter-only simulations shallower, and induce DM halos with a central mass distribution similar to that observed in nearby dwarf galaxies.

Subject headings: Galaxies: dark matter halos – galaxies: cosmological N-body+SPH simulations – galaxies: kinematics and dynamics

1. INTRODUCTION

The dark matter (DM) distributions at the centers of galaxies have been intensively discussed from both observational and theoretical sides for almost two decades ever since high-resolution N-body dark matter simulations assuming a universe dominated by cold dark matter (CDM) and a cosmological constant Λ were performed. The ΛCDM simulations have invariably predicted a dark matter density distribution which diverges toward the centers of galaxies (Moore 1994; Navarro, Frenk & White 1996, 1997; Moore et al. 1999b; Ghigna et al. 2000; Klypin et al. 2001; Power et al. 2002; Stoehr et al. 2003; Navarro et al. 2004; Reed et al. 2005; Diemand et al. 2008). In order to describe such cusp–like dark matter distributions, Navarro, Frenk and White (1995; 1996) proposed a profile (hereafter NFW profile) which can be approximated by two power laws, $\rho \sim r^{-1.0}$ and $\rho \sim r^{-3.0}$ to describe the inner and outer regions of a dark matter halo, respectively. In particular, the central cusp feature with $\rho \sim r^{-1.0}$ has provided a useful test for ΛCDM cosmology and sparked interest in seeking constraints by observing mass distributions at the center of galaxies (e.g., McGaugh et al. 2003). It is worth mentioning that recent simulations show shallower slopes with $\alpha \sim -0.8$ at radii of 120 pc (Stadel et al. 2009) although DM slopes at $r < 1$ kpc are generally steeper (see also Navarro et al. 2010).

The prediction of a central cusp from the ΛCDM model has been seriously challenged by observations of dwarf and Low Surface Brightness (LSB) disk galaxies. Observations of dwarf and LSB galaxies generally indicate a constant matter distribution toward their centers, with mass density profiles with a kpc sized core radius. This discrepancy of central dark matter distributions in dwarf galaxies in ΛCDM simulations and observations is referred to as the "cusp/core" problem. This is a fundamental problem for ΛCDM together with the likely connected substructure and angular momentum problems (Moore et al. 1999a; Klypin et al. 1999; Simon & Geha 2007; Navarro & White 1994; Dutton 2009).

Compared to other types of galaxies, dwarf galaxies provide us with a good opportunity for measuring the dark matter distribution near the centers of galaxies due

Electronic address: seheon_oh@ast.uct.ac.za
Electronic address: cbbrook@uclan.ac.uk
Electronic address: fabio@astro.washington.edu
Electronic address: E.Brinks@herts.ac.uk
Electronic address: lmayer@physik.unizh.ch
Electronic address: edeblok@ast.uct.ac.za
Electronic address: abrooks@tapir.caltech.edu
Electronic address: walter@mpia.de
[1] Astronomy Department, Astrophysics, Cosmology and Gravity Centre (ACGC), University of Cape Town, Private Bag X3, Rondebosch 7701, South Africa
[2] Jeremiah Horrocks Institute, University of Central Lancashire, Preston, Lancashire, PR1 2HE, United Kingdom
[3] Astronomy Department, University of Washington, Seattle, Washington 98195, USA
[4] Centre for Astrophysics Research, University of Hertfordshire, College Lane, Hatfield, AL10 9AB, United Kingdom
[5] Institute for Theoretical Physics, University of Zurich, Winterthurestrasse 190, 8057 Zürich
[6] Theoretical Astrophysics, California Institute of Technology, MC 350-17, Pasadena, California 91125, USA
[7] Max-Planck-Institut für Astronomie, Königstuhl 17, 69117 Heidelberg, Germany
[8] Square Kilometre Array South African Fellow

to the fact that they have a simple dynamical structure (disk galaxies without bulges) but also have low baryon fractions and hence less of a dynamical contribution by baryons (de Blok & McGaugh 1997). Recently, Oh et al. (2011) presented high-resolution dark matter density profiles of 7 dwarf galaxies taken from "The HI Nearby Galaxy Survey" (THINGS; Walter et al. 2008). The high quality data from THINGS significantly minimizes observational uncertainties and thus allows us to investigate the central dark matter distribution of the dwarf galaxies in detail. Mass models of stars and gas are constructed using the *Spitzer* IRAC 3.6μm data from the "*Spitzer* Infrared Nearby Galaxies Survey" (SINGS; Kennicutt et al. 2003) and the total integrated THINGS HI map, respectively. The kinematics of baryons are then subtracted from the total kinematics of the galaxies in order to derive the dark matter distributions.

One of the main results of Oh et al. (2011) was to robustly confirm that the rotation curves of the 7 THINGS dwarf galaxies rise too slowly to be consistent with a cusp feature at their centers. Moreover, the mean value of the logarithmic inner slopes of the dark matter density profiles is $\alpha = -0.29 \pm 0.07$, which significantly deviates from the $\alpha \sim -1.0$ predicted from dark-matter-only simulations. The exquisite data used in this study allowed unprecedented treatment of the effects of observational uncertainties, such as beam smearing, center offset and non-circular motions, which may play a role in hiding central cusps (Blais-Ouellette et al. 1999; van den Bosch et al. 2000; Bolatto et al. 2002; Swaters et al. 2003; Simon et al. 2003; Rhee et al. 2004; Gentile et al. 2005; Spekkens et al. 2005; Oh et al. 2008). The results have thus significantly strengthened the observational evidence that the dark matter distribution near the centers of dwarf galaxies follows a near–constant density core.

Before using these results as a repudiation of cold dark matter, however, one must also examine carefully the modeling on which the central cusp predictions are based, which are usually done using N-body simulations that include only the effects of gravity on structure formation. Although baryons make up only ∼14% of the matter of the Universe, this dissipative constituent of the Universe cools with cosmological time and accumulates in the central regions of DM halos, making up a dynamically important fraction. Several mechanisms have been proposed whereby these central baryons can affect the central cusp–like dark matter distribution which is found in pure dark matter simulations. A rapid change in potential (faster than the dynamical time) due to star burst triggered outflows, is one mechanism which has been shown to be capable of transforming cusp–like profiles into (flatter) cores (Navarro et al. 1996; Read & Gilmore 2005 although see Gnedin & Zhao 2002). Supernova driven random bulk motions of gas in proto-galaxies (Mashchenko et al. 2006) has also been shown in models to flatten cusps, as have the effects of dynamical friction acting on gas clumps (El-Zant et al. 2002), and the transfer of angular momentum from baryons to the dark matter (Tonini et al. 2006). Modeling an inhomogeneous multi–phase, interstellar medium is critical for simulating the baryonic feedback processes in galaxies (Robertson & Kravtsov 2008; Ceverino & Klypin 2009). Yet cosmological simulations have not, until recently, been able to achieve enough resolution to model even such an inhomogeneous ISM, but have been forced to treat the important processes of star formation and feedback as "sub-grid" physics, averaging star formation and supernova feedback over large volumes, compared to the typical structural scales (<1 kpc) of small galaxy disks.

Most recently, Governato et al. (2010) have performed high-resolution cosmological N–body+Smoothed Particle Hydrodynamic (SPH) simulations of dwarf galaxies under the ΛCDM paradigm, that include the effect of baryonic feedback processes, such as gas cooling, star formation, cosmic UV background heating and most importantly physically motivated gas outflows driven by SNe. The major finding of Governato et al. (2010) was that once star formation is associated with high density gas regions, a significant amount of baryons with low angular momentum is efficiently removed by strong SNe–driven injection of thermal energy and the following gas outflows that carry an amount of gas at a rate of 2–6 times the local star formation rate. The large scale outflows in turn induce two effects: the loss of low angular momentum gas from the central regions prevents the formation of bulges in low mass systems. Secondly, the clumpy nature of the gas and rapid ejection on short timescales has dynamical effects on the dark matter potential, creating a shallower density profile (see Mashchenko et al. 2008; Ceverino & Klypin 2009; Mo & Mao 2004; Mashchenko et al. 2006).

Moreover, the simulated galaxies have a z=0 baryonic budget consistent with photometric and kinematic estimates (van den Bosch et al. 2001; McGaugh et al. 2010). The kinematic properties of the simulated dwarf galaxies are very similar to those of the THINGS dwarf galaxies in terms of their maximum rotation velocity (∼60 km s^{-1}) and dynamical mass (∼10^9 $M_\odot$), allowing a direct comparison between the simulations and observations to be made.

A first estimate of the bulge-to-disk ratio and DM properties of these models was presented in Governato et al. (2010) by fitting a Sersic profile to artificial i–band images and fitting a rotation curve to the rotational motions of cold gas using a tilted-ring analysis. Here, we make more direct comparisons with observations, *applying the same analysis techniques and tools* to the simulations as done in the most recent observational sample of analoguous galaxies. The determination of the DM slopes for the simulations has to be done in the same way as in observations since there are various aspects that can affect the answer, such as beam smearing, center offset and non-circular motions, which were not taken into account when the slope was derived from the raw simulation data in Governato et al. (2010). This approach will have two crucial benefits: (1) provide a strong test of theoretical predictions and (2) test the extent of observational biases possibly associated to current models of baryon/DM mass decompositions in real galaxies, in particular the recovery of non-circular motions and pressure support induced by SN feedback (Valenzuela et al. 2007; Dalcanton & Stilp 2010).

The structure of this paper is as follows. The simulations are described in Section 2. In Section 3, we present the dark matter mass modeling of the simulated dwarf galaxies. Section 4 compares the derived dark matter distributions from the simulations with those of the

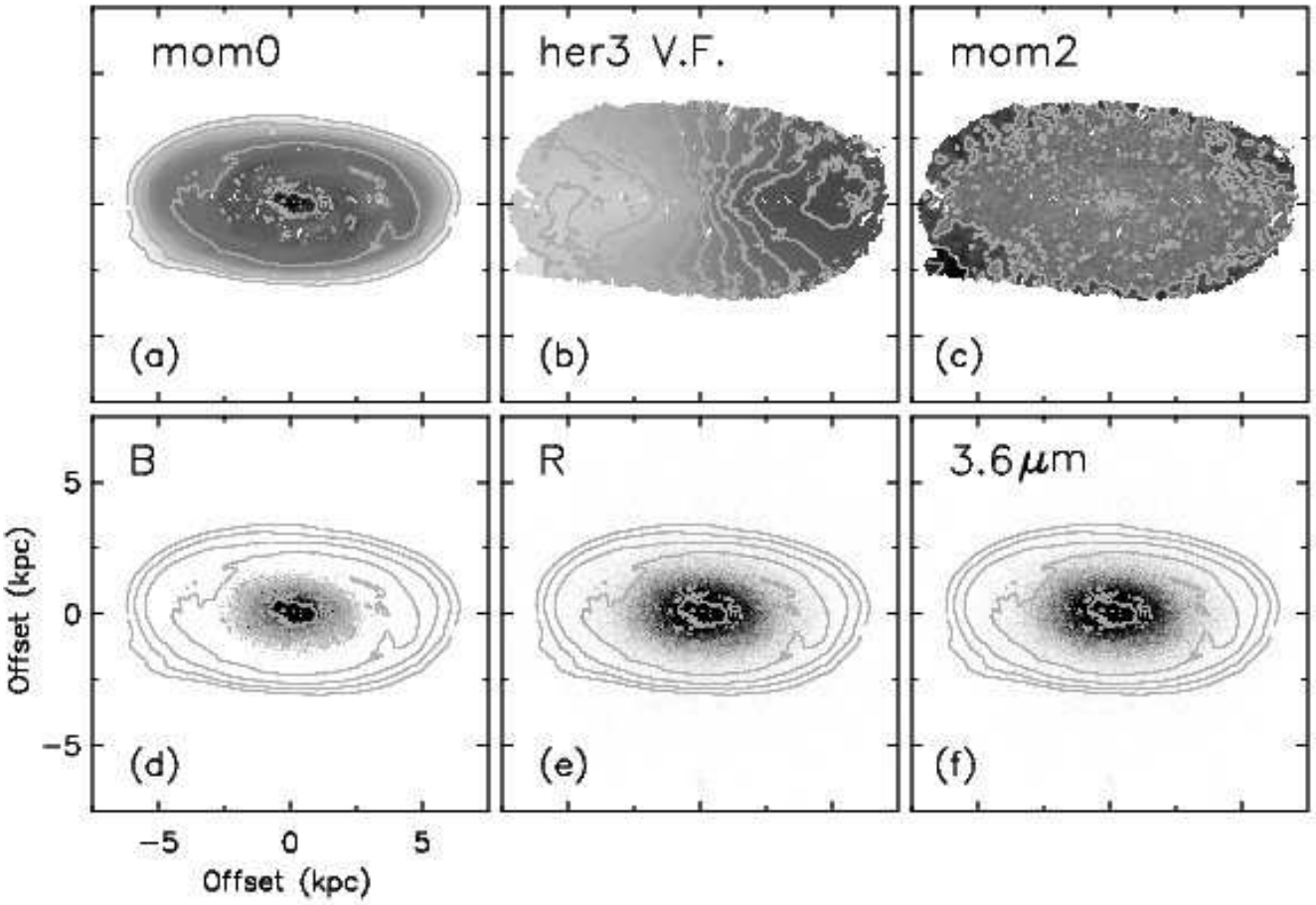

FIG. 1.— Gas and stellar components of DG1. **(a):** Simulated integrated gas map (moment 0). Contours start from a column density of 10^{20} cm^{-2} to 10^{22} cm^{-2} in steps of $10^{0.4}$ cm^{-2}. **(b):** Hermite h_3 velocity field. Velocity contours run from -50 km s^{-1} to 50 km s^{-1} with a spacing of 10 km s^{-1}. **(c):** Velocity dispersion map (moment 2). Velocity contours run from 5 km s^{-1} (gray) to 15 km s^{-1} (black) with a spacing of 4 km s^{-1}. **(d)(e)(f):**: Total intensity maps in simulated optical B, R and Spitzer IRAC 3.6 μm bands with superimposed contours of the gas map in the panel (a).

THINGS dwarf galaxies. Lastly, we summarize the main results of this paper and conclusions in Section 5.

2. THE SPH TREECODE GASOLINE

The halos for these simulations were selected from a set of large–scale, low–resolution, dark matter only simulation run in a concordance, flat, Λ-dominated cosmology: $\Omega_0 = 0.24$, Λ=0.76, $h = 0.73$, $\sigma_8 = 0.77$, and $\Omega_b = 0.042$ (Verde et al. 2003). The size of the box, 25 Mpc, is large enough to provide realistic torques for the small galaxies used in this work. The power spectra to model the initial linear density field were calculated using the CMBFAST code to generate transfer functions. To include the effects of cosmic torques from the large scale structure we used the volume renormalization (or "zoom in") technique (Katz & White 1993). Dark matter particle masses in the high resolution regions are 1.6×10^4 M$_\odot$, while the mass of star particles is only 1000 M$_\odot$ and the force resolution, i.e., the gravitational softening, is 86 pc. In total, at z=0 there are 3.3×10^6 particles within the virial radius of the simulated dwarf galaxy, hereafter referred to as DG1. For all particle species, the gravitational spline softening, $\epsilon(z)$, was evolved in a comoving manner from the starting redshift (z $\sim$ 100) until z=8, and then remained fixed at its final value from z=8 to the present. At z = 0 the virial masses of the halos that we studied in this paper are 3.5 (DG1) and 2.0 (DG2) $\times$ 10^{10} M$_\odot$ (the virial mass is measured within the virial radius R$_{\rm vir}$, the radius enclosing an overdensity of 100 times the cosmological critical density).

To evolve the simulations described here we have used the fully parallel, N-body+SPH code GASOLINE to compute the evolution of both the collisionless and dissipative component in the simulations. A detailed description of the code is available in the literature (Wadsley et al. 2004). The version of the code used in this paper includes radiative cooling and accounts for the effect of a uniform background radiation field on the ionization and excitation state of the gas. The cosmic ultraviolet background is implemented using the Haardt-Madau model (Haardt & Madau 1996), including photoionizing and photoheating rates produced by PopIII stars, QSOs and galaxies starting at $z = 9$. We use a standard cooling function for a primordial mixture of atomic hydrogen and helium at high gas temperatures and we include low temperature cooling (Mashchenko et al. 2006).

In the simulations described in this paper star formation occurs when cold gas reaches a given threshold density (e.g., Stinson et al. 2006) typical of actual star forming regions (we used 100 atomic–mass–unit (amu) cm^{-3}). Star formation (SF) then proceeds at a rate proportional to $\rho_{gas}^{1.5}$, i.e. locally enforcing a Schmidt law. The adopted

feedback scheme is implemented by releasing thermal energy from SNe into the gas surrounding each star particle (Stinson et al. 2006). The energy release rate is tied to the time of formation of each particle (which effectively ages as a single stellar population with a Kroupa IMF). To model the effect of feedback at unresolved scales, the affected gas has its cooling shut off for a time scale proportional to the Sedov solution of the blast wave equation, which is set by the local density and temperature of the gas and the amount of energy involved. The effect of feedback is to regulate star formation in the discs of massive galaxies and to greatly lower the star formation efficiency in galaxies with peak circular velocity in the 50 $< V_c <$150 km s^{-1} range (Brooks et al. 2007). At even smaller halo masses ($V_c <$ 20-40 km s^{-1}) the collapse of baryons is largely suppressed by the cosmic UV field (Quinn et al. 1996; Okamoto et al. 2008; Gnedin 2010).

Other than the density threshold only two other parameters are needed, the star formation efficiency (ϵSF = 0.1) and the fraction of SN energy coupled to the ISM (ϵSN=0.4). The model galaxies studied in this paper are those published in Governato et al. (2010). We verified that the addition of full metal cooling and the increase of ϵSN to 1 does not substantially change the structural properties of the galaxy. However the amount of stars formed decreases by 40%.

As a benchmark against which the effects of baryonic feedback processes can be gauged, Governato et al. (2010) performed additional runs for analoguous model galaxies of DG1, called DG1DM and DG1LT. DG1DM uses the same initial conditions as DG1 but includes only the dark matter component. It has a DM slope of $\alpha \sim -1.3$ similar to those found from similar simulations (Springel et al. 2008). DG1LT is a version of DG1 using a lower density threshold (0.1 amu cm^{-3}) at a lower resolution (the force resolution is ∼116 pc), and outflows in this model are negligible. DG1LT has a cusp and its DM slope is similar to that of DG1DM ($\alpha \sim -1.3$).

To properly compare the outputs from the simulation to real galaxies and make accurate estimates of the *observable* properties of galaxies (e.g., Sánchez-Janssen et al. 2010), we used the Monte Carlo radiation transfer code *SUNRISE* (Jonsson et al. 2010) to generate artificial optical images and spectral energy distributions (SEDs) of the outputs of our run. *SUNRISE* allows us to measure the dust reprocessed SED of every resolution element of the simulated galaxies, from the far UV to the far IR, with a full 3–D treatment of radiative transfer. We place the simulated galaxies at an inclination of 60 degrees. However, in applying our analysis tools, the inclination is considered a free parameter, in keeping with the techniques applied to observed galaxies. Filters mimicking those of the SDSS survey are used to create mock observations.

We note that in the runs adopting the "high threshold" SF, feedback produces winds that are comparable in strength to those found in real galaxies of similar mass. However, in our simulations the cold ISM is still only moderately turbulent (∼ 5–10 km s^{-1} at z = 0), consistent with observations, and the galaxies match the observed stellar and baryonic Tully–Fisher relation (Governato et al. 2009), as the SF efficiency is regulated to form an amount of stars similar to that of real dwarf galaxies of similar rotation velocity.

In the following sections, we perform dark matter mass modeling of both DG1 and DG2 in exactly the same way as the THINGS dwarf galaxies sample described in Oh et al. (2008, 2011).

3. THE MASS MODELING OF THE SIMULATED DWARF GALAXIES

3.1. *The rotation curves*

We first construct the data cubes of DG1 and DG2 by tracing the motions of the gas component. The beam and velocity resolutions of the cubes are ∼6″ (corresponding to 100 pc at a distance of 4 Mpc) and 2.0 km s^{-1}, respectively. As an example, we show the integrated gas map, velocity field and velocity dispersion map extracted from the cube for DG1 in Fig. 1. For the velocity field, we use the Gauss-Hermite polynomial to model the skewness of a non-Gaussian profile caused by multiple velocity components (van der Marel & Franx 1993). This function includes an extra parameter, called h_3, that measures the skewness of the Gaussian function, and thus provides more reliable central velocities even for profiles with significant asymmetries. As discussed in Oh et al. (2011) (see also de Blok et al. 2008), the hermite h_3 velocity field gives a robust estimate for the underlying circular rotation of a galaxy in which non-circular motions are insignificant, like DG1 and DG2. Hermite h_3 polynomials have also been used to extract the velocity fields of the THINGS galaxies sample (de Blok et al. 2008).

Oh et al. (2011) use the bulk velocity fields when deriving the rotation curves of the THINGS dwarf galaxies, except for DDO 154 and M81dwB in which non-circular motions are insignificant. Compared to other types of velocity fields (e.g., intensity-weighted mean, hermite h_3, single Gaussian and peak velocity fields), the bulk velocity field more effectively minimizes the effect of small-scale random motions on the derived kinematics of a galaxy (see Oh et al. 2008 for details). However, for a galaxy that is not significantly affected by non-circular motions like DG1 and DG2, the bulk velocity field is nearly identical to the hermite h_3 velocity field.

In Fig. 1b, the iso-velocity contours of the extracted hermite h_3 velocity field are distorted in some regions, suggestive of non-circular motions. These are mainly due to the SN-driven gas outflows in the simulations. However, despite the presence of non-circular motions the overall pattern of the galaxy rotation is well recovered in the velocity field.

It is customary to use a set of concentric tilted-rings to model the velocity field of a galaxy, each with its own kinematic center (XPOS, YPOS), inclination INCL, position angle PA, expansion velocity VEXP, systemic velocity VSYS and rotation velocity VROT (Begeman 1989). PA is the angle measured counter-clockwise from the north direction in the sky to the major axis of the receding half of the galaxy.

Assuming an infinitely thin disk, we fit these tilted-rings to the hermite h_3 velocity fields of DG1 and DG2 to derive their rotation curves. The derived tilted-ring models for DG1 and DG2 are shown in Fig. 2. The errorbar in the rotation velocities indicates the dispersion of individual velocity values found along a tilted-ring. As mentioned earlier, gas outflows driven by SN explosions in the simulations cause non-circular motions at some regions and induce larger uncertainties in the fit-

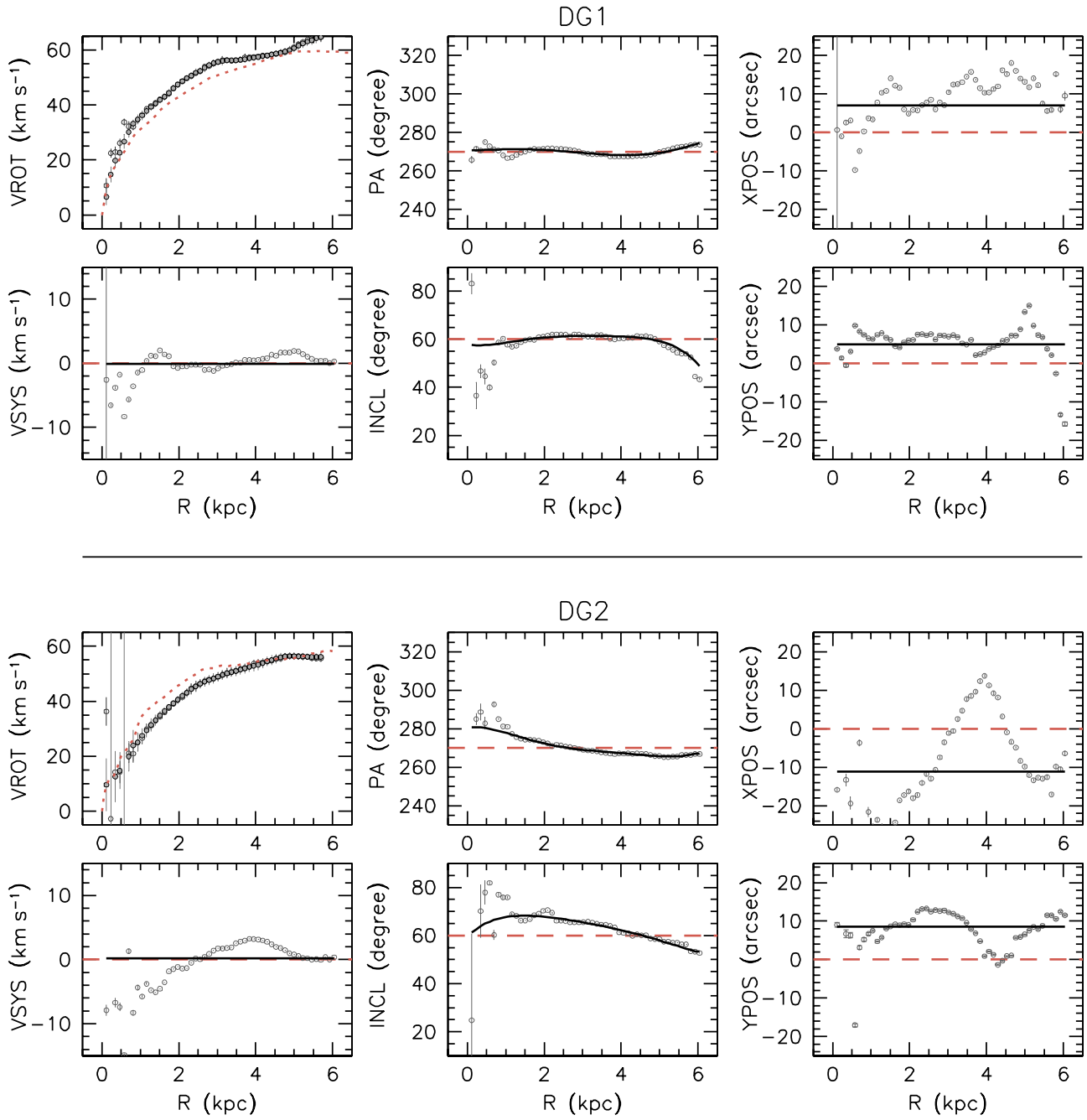

FIG. 2.— The tilted-ring models derived from the hermite h_3 velocity fields of DG1 (upper) and DG2 (lower). The open circles in all panels indicate the fit made with all parameters free. The filled black circles and solid lines in all panels show the finally adopted tilted-ring models as a function of galaxy radius. The dashed lines indicate the geometrical parameters used when extracting the rotation velocities (dotted lines in the VROT panels) from the true mass distributions of the simulated galaxies.

ted tilted-rings. These are seen as the scatter of the very first run results (open circles) with all ring parameters free in Fig. 2. However, the local scatter averages out after several iterations and the final rotation curves (solid lines) in Fig. 2 seem to give a good description of the underlying kinematics of DG1 and DG2. As shown in the VROT panels of Fig. 2, this can be confirmed by the true rotation velocities (dotted lines) derived using the full three dimensional mass distributions rather than the projected two dimensional surface density profiles of the simulated galaxies. Despite not only the uncertainties but also the assumption of the tilted-ring analysis, i.e., an infinitely thin disk, the difference between the true and derived rotation velocities is less than 5 km s^{-1}, equivalent to about twice the velocity resolution of the cubes.

For galaxies whose velocity dispersions are large enough compared to their maximum rotation velocities, we need to correct for the asymmetric drift to obtain more reliable rotation velocities (Bureau & Carignan 2002). However, the 2nd moment maps of DG1 and DG2 show small velocity dispersions ($\sim$7 km s^{-1}) compared to the maximum rotation velocities ($\sim$60 km s^{-1}), and the pressure support is insignificant with respect to the circular rotations. Therefore, we ignore the asymmetric drift corrections for DG1 and DG2.

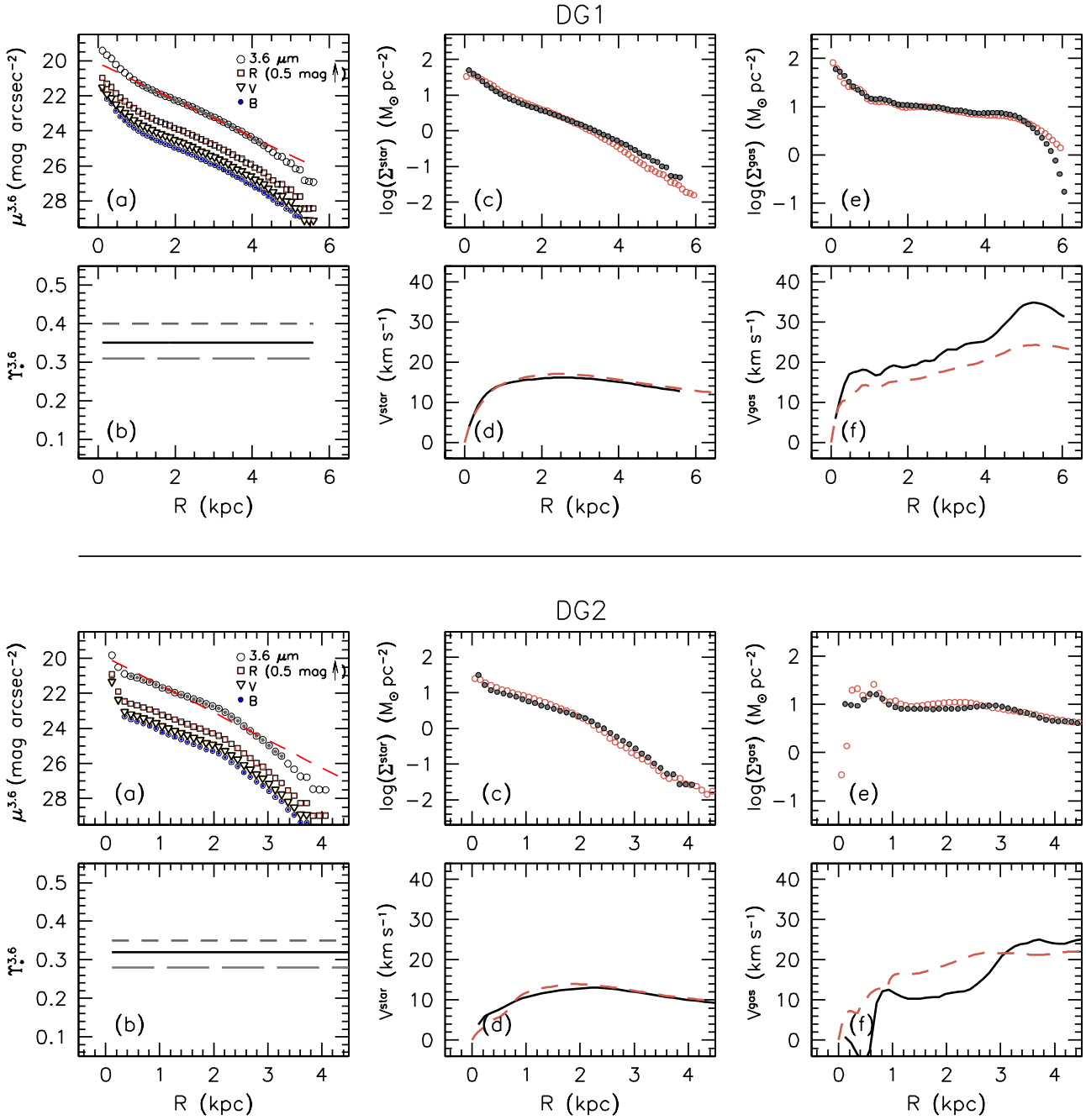

FIG. 3.— Mass models for the baryons of DG1 (top) and DG2 (bottom). **(a):** Azimuthally averaged surface brightness profiles (corrected for inclination) in the simulated 3.6μm, R, V, and B bands (top to bottom) derived applying the tilted-ring parameters shown in Fig. 2. Note that the R-band surface brightness profile is shifted upward by 0.5 mag for clarity. The dashed line for the 3.6μm profile indicates a least-squares fit to the data, the radial range over which the fit is made being indicated by the filled circles. **(b):** The $\Upsilon_\star$ in the 3.6μm band derived from stellar population synthesis models. The short and long dashed lines show the $\Upsilon_\star^{3.6}$ values derived using optical colors $B-V$ and $B-R$, respectively. The solid line indicates the mean value adopted as the final $\Upsilon_\star^{3.6}$. **(c):** The stellar mass surface density derived from the 3.6μm surface brightness in (a) using the $\Upsilon_\star^{3.6}$ value shown in the panel (b). The red open circles indicate the true profile derived from the simulations. **(d):** The rotation velocity for the stellar component derived from the stellar mass density profile (dots) in the panel (c). The dashed line shows the true rotation velocity for the stellar component derived from the true profile (open circles) shown in the panel (c). **(e):** The radial mass surface density distribution of the gas component scaled by 1.4 to account for He and metals. The red open circles indicate the true profile derived from the simulations. **(f):** The gas rotation velocity derived from the gas surface density profile (dots) in the panel (e). The dashed line shows the true rotation velocity for the gas component derived from the true profile (open circles) shown in the panel (e).

TABLE 1
PROPERTIES OF THE SIMULATED AND THE THINGS DWARF GALAXIES

Name	D (Mpc) (1)	⟨Incl.⟩ (°) (2)	z_0 (kpc) (3)	M_B (mag) (4)	V_{max} (km s^{-1}) (5)	R_{max} (kpc) (6)	M_{dyn} ($10^9\,M_\odot$) (7)	M_{halo} ($10^9\,M_\odot$) (8)	M_{star} ($10^8\,M_\odot$) (9)	M_{gas} ($10^8\,M_\odot$) (10)
IC 2574	4.0	55.7	0.57	-18.1	77.6	10.4	14.6	53.2	10.38	18.63
NGC 2366	3.4	39.8	0.34	-17.2	57.5	5.6	4.3	76.9	2.58	6.98
Holmberg I	3.8	13.9	0.55	-14.8	38.0	1.5	0.5	33.1	1.25	2.06
Holmberg II	3.4	49.6	0.28	-16.9	35.5	7.1	2.1	4.3	2.00	7.41
M81 dwB	5.3	44.8	0.09	-14.2	39.8	0.8	0.3	870.9	0.30	0.31
DDO 53	3.6	27.0	0.14	-13.4	32.4	2.0	0.5	2.1	0.18	0.85
DDO 154	4.3	66.0	0.20	-14.2	53.2	8.2	5.4	2.4	0.26	3.58
DG1	4.0	60.0	0.41	-15.9	60.0	5.0	4.2	35.0	1.81	8.04
DG2	4.0	60.0	0.28	-15.6	56.4	5.0	3.7	20.0	0.80	5.92

NOTE. — **(1):** Distance as given in Walter et al. (2008). For DG1 and DG2, we assume they are at a distance of 4 Mpc; **(2):** Average value of the inclination derived from the tilted-ring analysis; **(3):** The vertical scale height of disk; **(4):** Absolute B magnitude as given in Walter et al. (2008); **(5):** Maximum rotation velocity; **(6):** The radius where the rotation velocity V_{max} of the flat part of the rotation curve is measured; **(7):** Dynamical mass from the measured V_{max} and R_{max}. **(8):** Halo mass M_{200} determined from V_{200} using Eq. 3. For the THINGS dwarf galaxies we use the V_{200} values fitted using c fixed to 5. See Section 4.1 for more details. For DG1 and DG2, we show the virial mass measured within the virial radius R_{vir} enclosing an overdensity of 100 times the cosmological critical density; **(9):** Stellar mass derived in Section 3.2. The stellar mass of DDO 154 is from de Blok et al. (2008); **(10):** Gas mass derived in Section 3.2. The gas mass of DDO 154 is from Walter et al. (2008).

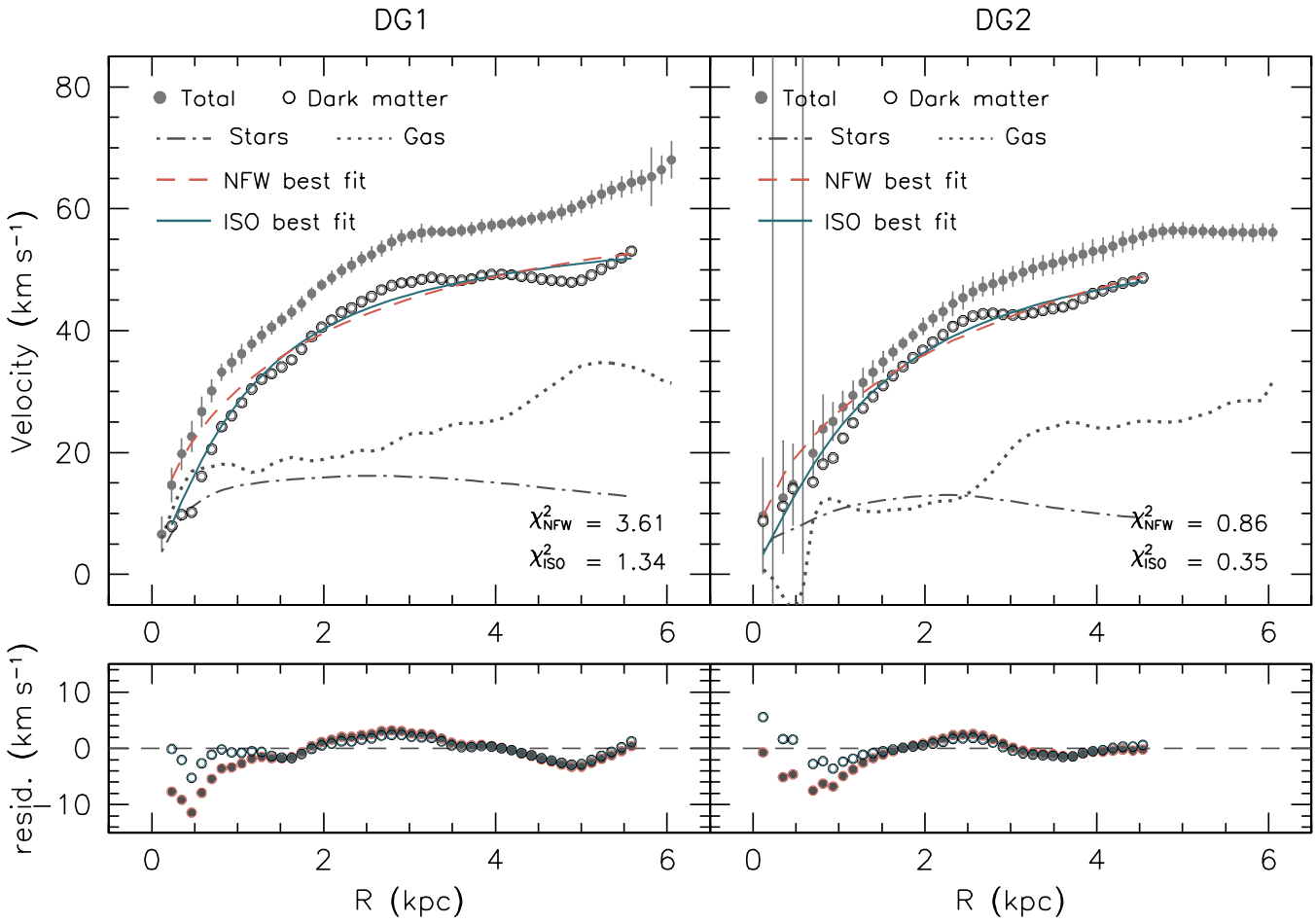

FIG. 4.— The Disk-halo decompositions of the rotation curves of DG1 (left) and DG2 (right). The gray dots represent the total rotation curves derived from the hermite h_3 velocity fields. The dotted and dash-dotted lines indicate the rotation curves of the gas and stellar components, respectively. The open circles show the dark matter rotation curves derived subtracting the rotation curves of baryons from the total rotation curves. The dashed and solid lines show the best fitted NFW and pseudo-isothermal halo models to the dark matter rotation curves, respectively. The reduced χ^2 value for each halo model is denoted on the panels. The lower panels show the velocity residuals between the dark matter rotation curves and the best fitted halo models. The dots and open circles indicate the results from the NFW and pseudo-isothermal halo models, respectively.

3.2. *The mass models of baryons*

The derived rotation curves in the previous section represent the total kinematics of the galaxies, including not only dark matter but also the stellar and gas components. We therefore construct mass models of the baryons and subtract them from the total kinematics to separate the dark matter component only.

For the gas component, we first derive the gas surface density profile by applying the derived tilted-rings in Section 3.1 to the integrated gas map shown in the upper-left panel of Fig. 1. The derived gas surface density profile is then scaled by a factor of 1.4 to account for helium and metals. The resulting gas surface density profiles of DG1 and DG2 are given in panels (e) of Fig. 3. From these, we calculate the rotation velocity due to the gas component, assuming an infinitely thin disk. The derived gas rotation velocities of DG1 and DG2 are shown in panels (f) of Fig. 3. We also overplot the true values derived using the full three dimensional mass distribution of the gas components of DG1 and DG2 as shown in the open circles in the panels (e) of Fig. 3. For DG1, the true and derived gas surface density profiles are similar but the derived rotation velocity is systematically higher than the true one. This can be due to the assumption of "an infinitely thin disk[1]" which makes one overestimate the gas rotation velocity of a galaxy with a considerable gas thickness. However, the velocity difference ($\sim$5 km s^{-1}) is not very significant. For DG2, the true gas velocity is systematically higher in the range 0–3 kpc, particularly in the inner region. Likewise, the true surface density profile is higher than the derived one in the range 0–3 kpc. As shown in Fig. 2, this is partially because the smaller inclination value (60°) is used for extracting the true gas surface density profile from the simulation in the inner region of DG2. In addition this may also be due to significant vertical gas outflows or flaring driven by SNe perpendicular to the disk of the galaxy.

Similar to the gas component, we derive the surface density profiles for the stellar components of DG1 and DG2. For this, as shown in Fig. 1, we use the simulated B, V, R and *Spitzer* IRAC1 3.6μm images. In particular, the *Spitzer* IRAC1 3.6μm image is useful for tracing the underlying old stars which are usually the dominant stellar population in dwarf galaxies. For the same reason, *Spitzer* IRAC 3.6μm images have also been used for making mass models for the stellar components of the THINGS galaxies sample (de Blok et al. 2008; Oh et al. 2008, 2011).

We derive the surface brightness profiles of DG1 and DG2 by applying the tilted-rings derived in Section 3.1 to their simulated B, V and R as well as 3.6μm images. Both DG1 and DG2 are bulgeless as found from fitting a Sersic profile to their i band images (Governato et al. 2010). To convert the surface brightness profiles to the mass density profiles in units of M$_\odot$ pc^{-2}, we obtain the 3.6μm mass-to-light ($\Upsilon_\star^{3.6}$) values using an empirical relation between $\Upsilon_\star^{3.6}$ and optical colors based on the Bruzual & Charlot (2003) stellar population synthesis models (Oh et al. 2008; see also Bell & de Jong 2001).

[1] The gas rotation velocities assuming "an exponential density law" with scale heights in the range of 0.5–2.5 kpc are somewhat similar to the true one but slightly higher in the outer regions, possibly due to SNe-driven gas outflows or flaring.

The $\Upsilon_\star^{3.6}$ values used for DG1 and DG2 are shown as the solid lines in panels (b) of Fig. 3, and the resulting stellar surface density profiles are given in panels (c) of Fig. 3. The true surface density profiles for the stellar components of DG1 and DG2 are also overplotted as the open circles in Fig. 3, and they are similar to the derived ones. This can be treated as circumstantial evidence that the assumption used for the stellar distribution and $\Upsilon_\star^{3.6}$ values provide a good description for the stellar components of DG1 and DG2.

From these, we then compute the corresponding stellar rotation velocities assuming a vertical sech$^2(z)$ scale height distribution of stars. We calculate the vertical scale height z_0 using a ratio of h/z_0=2.5 where h is the radial scale length of disk, derived from the 3.6μm surface brightness profile. The derived scale heights z_0 of DG1 and DG2 are 0.41 kpc and 0.28 kpc, respectively. These are similar to the mean value (0.32 kpc) of the 7 THINGS dwarf galaxies as given in Oh et al. (2011). The derived stellar rotation velocities of DG1 and DG2 are shown in panels (d) of Fig. 3, and they agree well with the true ones indicated by dashed lines.

3.3. *The disk-halo decomposition*

We separate the dark matter components of DG1 and DG2 by subtracting the mass models of baryons derived in Section 3.2 from their total rotation curves. We then fit two halo models, the NFW and pseudo-isothermal (ISO) halo models, to these kinematic residuals in order to examine the dark matter distribution in a quantitative way. The NFW and pseudo-isothermal halo models represent cusp–like and constant density (core) matter distributions at the centers of galaxies, respectively.

The NFW halo model (Navarro et al. 1996, 1997) is given as,

$$V_{\rm NFW}(R) = V_{200}\sqrt{\frac{\ln(1+cx) - cx/(1+cx)}{x[\ln(1+c) - c/(1+c)]}}, \qquad (1)$$

where c is the parameter quantifying the degree of concentration of the dark matter halo. V_{200} is the rotation velocity at radius R_{200} where the density contrast with the critical density of the Universe exceeds 200 and x is defined as R/R_{200}.

Likewise, the rotation velocity based on the pseudo-isothermal halo model is as follows,

$$V_{\rm ISO}(R) = \sqrt{4\pi G\rho_0 R_C^2\left[1 - \frac{R_C}{R}{\rm atan}\left(\frac{R}{R_C}\right)\right]}, \qquad (2)$$

where ρ_0 and R_C are the core-density and core-radius of a halo, respectively.

By comparing the fit qualities of these two halo models to the kinematic residuals for the dark matter component, we examine which halo model is preferred to describe the derived dark matter distributions of DG1 and DG2.

As shown in the upper panels of Fig. 4, compared to the CDM NFW halo model, despite its feasible fits, the pseudo-isothermal halo model gives a better description for the derived dark matter distributions of both DG1 and DG2 in terms of the fit quality (i.e., reduced χ^2 values). This is also confirmed by the velocity residuals

between the dark matter rotation curves and the best fitted halo models as shown in the lower panels of Fig. 4. The best fitted NFW halo models are too steep to match the inner regions of the dark matter rotation curves of DG1 and DG2.

4. THE SIMULATIONS VS. THINGS

In this section, we compare the derived dark matter distribution of DG1 and DG2 with that of the 7 THINGS dwarf galaxies. THINGS is a high spectral (≤ 5.2 km s^{-1}) and angular ($\sim 6''$) resolution HI survey for 34 nearby galaxies undertaken using the NRAO[2] Very Large Array (VLA) (Walter et al. 2008). THINGS is complemented with other data, such as from the *Spitzer* SINGS survey and ancillary optical B, V and R images taken with the KPNO 2.1m telescope (Kennicutt et al. 2003). These high-quality multi-wavelength data significantly reduce observational uncertainties and thus enable us to derive more reliable mass models of the galaxies.

Oh et al. (2011) performed the dark matter mass modeling of 7 dwarf galaxies in exactly the same way as for DG1 and DG2 as described in Section 3. Basic properties of the galaxies are listed in Table 1. In particular, the selected 7 THINGS dwarf galaxies have similar observational properties as DG1 and DG2, such as resolution ($\sim$150 pc at the distance of $\sim$4 Mpc), maximum rotation velocity (< 80 km s^{-1}), dynamical mass ($\sim 10^9\ M_\odot$) and scale height ($\sim$0.3 kpc). In addition the THINGS dwarf galaxies are not satellites and they have most likely only weakly interacted with larger systems, as are the cases of DG1 and DG2. Therefore, this allows us to make a direct comparison between the simulations and observations, and examine if the simulated dwarf galaxies are realistic compared to the dwarf galaxies in the local universe.

4.1. *The relation between $M_{\rm star}$ and $M_{\rm halo}$*

By comparing the stellar masses of DG1 and DG2 to their halo masses, we examine whether the star formation efficiency of DG1 and DG2 is comparable with that of real galaxies which have similar dynamical masses. This is important as the number of stars which form in small halos can put strong constraints on baryonic feedback and its effects.

It has been found that galaxies of smaller or larger halo masses with respect to the Milky Way appear to have inefficient star formation (Navarro & Steinmetz 2000; Governato et al. 2007; Li & White 2009). The low star formation efficiency in high mass galaxies is often attributed to AGN feedback (Ciotti & Ostriker 2001; Benson & Madau 2003), while the effects of supernovae are often invoked to explain the low star formation efficiency in low mass galaxies (Larson 1974; White & Rees 1978). Recently, Guo et al. (2010) derived the relation between halo mass and stellar mass from abundance matching by combining the stellar mass function from the Sloan Digital Sky Survey data release 7 (SDSS/DR7; Li & White 2009) with the halo/subhalo mass function from N-body ΛCDM simulations (Millenium and Millenium-II simulations; Springel et al. 2005; Boylan-Kolchin et al. 2009; see also De Lucia & Blaizot 2007 based on semi-analytic models). Similar methods and results are found in Conroy & Wechsler (2009), Moster et al. (2010) and Trujillo-Gomez et al. (2010).

[2] The National Radio Astronomy Observatory is a facility of the National Science Foundation operated under cooperative agreement by Associated Universities, Inc.

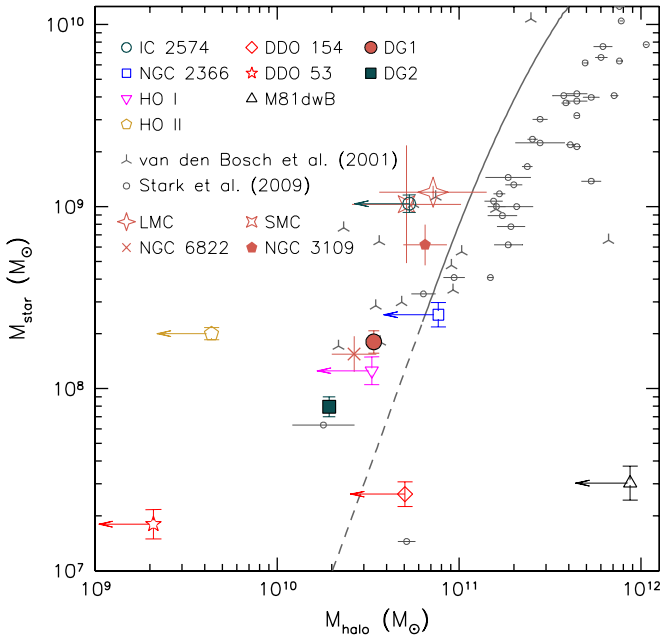

FIG. 5.— The $M_{\rm star}-M_{\rm halo}$ relation of DG1, DG2 and the THINGS dwarf galaxies (Oh et al. 2011) as well as galaxies from the literature (van den Bosch et al. 2001; Stark et al. 2009). The Local Group galaxies, LMC (Mastropietro et al. 2005; Guo et al. 2010), SMC (Stanimirović et al. 2004; Guo et al. 2010), NGC 6822 (Valenzuela et al. 2007) and NGC 3109 (Valenzuela et al. 2007) are also overplotted. The errorbars for $M_{\rm halo}$ and $M_{\rm star}$ of the LMC and SMC are computed based on the different estimates given by Guo et al. (2010) and the other two papers (i.e., Mastropietro et al. 2005 and Stanimirović et al. 2004). The errorbars for NGC 6822 and NGC 3109 come from the different mass models that Valenzuela et al. (2007) considered for these galaxies to reproduce their kinematical and photometrical properties assuming that they are hosted in CDM halos. The solid curve is from abundance matching by combining the stellar mass function from the SDSS/DR7 with the halo/subhalo mass function from the Millenium and Millenium-II simulations (Guo et al. 2010). As described in Guo et al. (2010), the relation below the stellar mass $10^{8.3}$ was extrapolated assuming constant slope as indicated by the dashed line. See Section 4.1 for more details.

Guo et al. (2010) have shown that the star formation efficiency in most recent hydrodynamical, cosmological galaxy formation simulations is higher than that predicted from the $M_{\rm star}-M_{\rm halo}$ relation. In particular, as shown in Fig. 5, the stellar masses of DG1 and DG2 are about an order of magnitude larger than those inferred from the relation.

However, since the SDSS/DR7 only covers the stellar mass range from $10^{8.3}$ to $10^{11.8}$, the $M_{\rm star}-M_{\rm halo}$ relation outside this range was extrapolated assuming a constant slope as indicated by the dashed line as shown in Fig. 5 (see Guo et al. 2010). The stellar masses of DG1 and DG2 fall within the lower extrapolated region. Here, we make a more direct comparison between the stellar mass to halo mass ratio between simulated and observed galaxies. To this end, we compare DG1 and DG2 with nearby low-mass galaxies from van den Bosch et al. (2001), Stark et al. (2009) and the local group as well as the 7 dwarfs from THINGS Oh et al. 2011).

For the halo mass of the THINGS dwarf galaxies, we

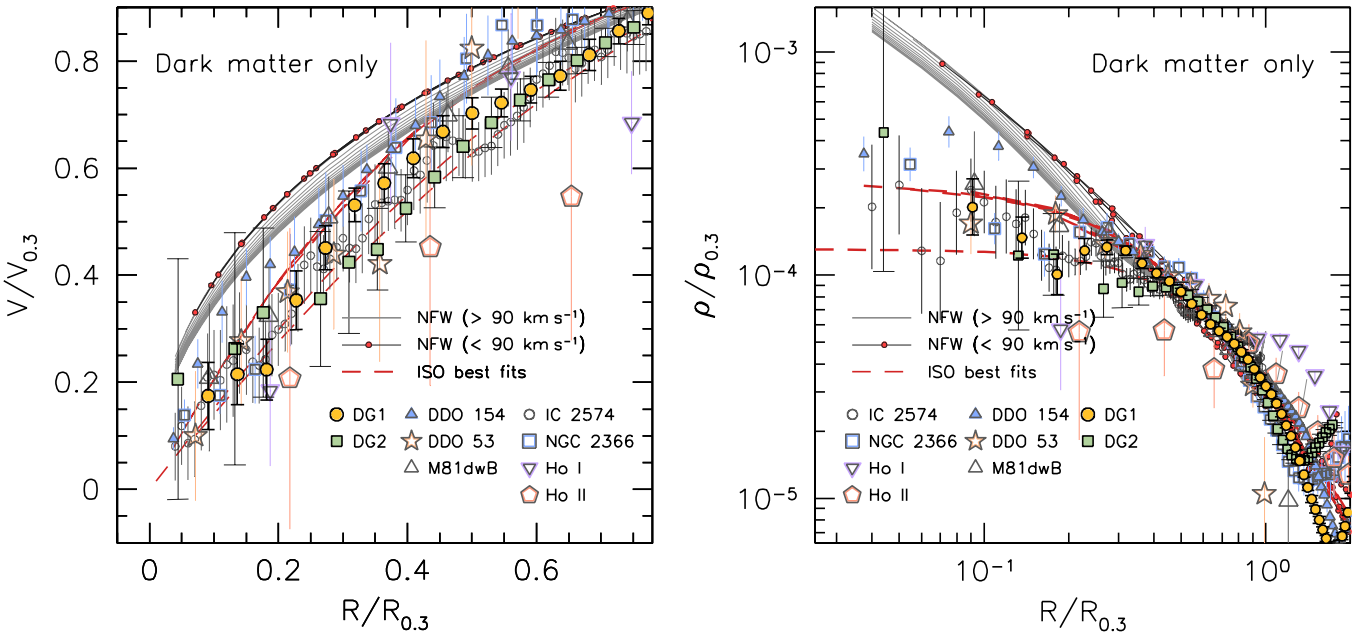

FIG. 6.— **Left:** The rotation curve shape of DG1 and DG2 as well as the 7 THINGS dwarf galaxies. The dark matter rotation curves (corrected for baryons as shown in Fig. 4) are scaled with respect to the rotation velocity $V_{0.3}$ at $R_{0.3}$ where the logarithmic slope of the curve is $d\log V/d\log R = 0.3$ (Hayashi & Navarro 2006). The small dots indicate the NFW model rotation curves with V_{200} ranging from 10 to 90 km s^{-1}. See text for further details. The best fitted pseudo-isothermal halo models (denoted as ISO) are also overplotted. See Section 4.2 for more details. **Right:** The scaled dark matter density profiles of DG1 and DG2 as well as the 7 THINGS dwarf galaxies. The profiles are derived using the scaled dark matter rotation curves in the left panel. The small dots represent the NFW models ($\alpha\sim-1.0$) with V_{200} ranging from 10 to 90 km s^{-1}. The dashed lines indicate the best fitted pseudo-isothermal halo models ($\alpha\sim0.0$). See Section 4.3 for more details.

estimate M_{200} as follows,

$$M_{200}\,[M_\odot] = 200 \times \frac{3H_0^2}{8\pi G} \times \frac{4\pi R_{200}^3}{3}$$
$$\simeq 100 \times \frac{H_0^2}{G} \times (\frac{V_{200}}{10H_0})^3$$
$$\simeq 3.29 \times 10^5 \times V_{200}^3, \quad (3)$$

where H_0 is the Hubble constant (70.6 km s^{-1} Mpc^{-1}; Suyu et al. 2010), G is the gravitational constant (4.3×10^{-3} pc M$_\odot^{-1}$ km^2 s^{-2}) and V_{200} in km s^{-1} is the rotation velocity at radius R_{200} as given in Eq. 1. However, the NFW halo model fails to fit the dark matter rotation curves of the THINGS dwarf galaxies, giving negative (or close to zero) c values (Oh et al. 2011). To circumvent the unphysical fits, we instead fit the NFW model to the rotation curves with only V_{200} as a free parameter after fixing c to 5 which is lower than typical values (e.g., 8–9; McGaugh et al. 2003) predicted from ΛCDM cosmology. The fitted V_{200} values of some galaxies are larger than their measured maximum rotation velocities. This is because the rotation curves are still rising at the last measured points. Moreover, as a larger c value induces a smaller V_{200} and hence lower halo mass, our choice of a low c will provide a robust upper limit for our derived halo mass, as indicated by the arrows in Fig. 5. As shown in Fig. 5, despite the uncertainties remaining in these estimates, the stellar masses of DG1 and DG2 at their given halo masses are consistent with those of real galaxies. Both the real galaxies and the simulations deviate from the extrapolated line from the $M_{\rm star}-M_{\rm halo}$ relation in Guo et al. (2010) at low halo masses. However, as discussed in Trujillo-Gomez et al. (2010), there still remain uncertainties for dwarfs in the sense that the observational data suffer from small number statistics and the results of abundance matching are incomplete in the low-luminosity tail of the luminosity function.

4.2. *The rotation curve shape*

The rotation curve reflects the total potential (dark matter + baryons) of the galaxy and thus it is directly related to the radial matter distribution in the galaxy (and vice versa). Consequently, the cusp–like dark matter distributions in the CDM halos impose a unique shape on the rotation curves, which steeply rise at the inner regions. Therefore, a relative comparison of galaxy rotation curves between the simulations and observations can serve as a useful constraint for testing the ΛCDM simulations.

In this context, we compare the rotation curves of DG1 and DG2 with those of the THINGS dwarf galaxies. In order to accentuate their inner shapes, we scale the rotation curves of both the simulations and the THINGS dwarf galaxies with respect to the velocity $V_{0.3}$ at the radius $R_{0.3}$ where the logarithmic slope of the curve is $d\log V/d\log R = 0.3$ (Hayashi & Navarro 2006). At the scaling radius $R_{0.3}$, the rotation curves of both simulations and the observations are well resolved, which allows any differences between them to show up.

The scaled rotation curves, with the kinematic contribution of baryons subtracted, are shown in the left panel of Fig. 6. We overplot the scaled rotation curves of NFW CDM halos (dark-matter-only) with different maximum rotation velocities ranging from 10 to 350 km s^{-1}. We choose c values of ∼9 and ∼8 for dwarf and disk galaxies respectively, which in turn provide V_{200} values ranging from ∼10 to ∼90 km s^{-1}, and ∼100 to ∼350 km s^{-1}, respectively. Considering that the rotation velocities of DG1, DG2 and the THINGS dwarf galaxies at the out-

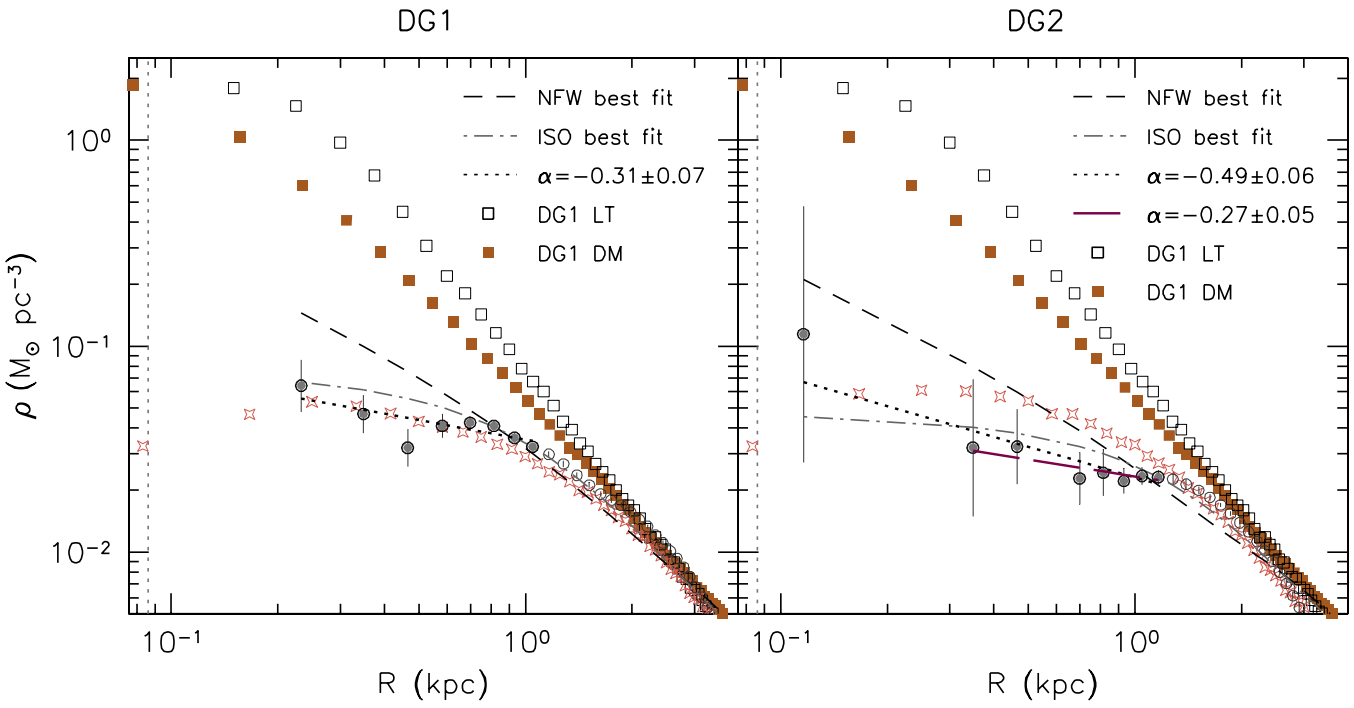

FIG. 7.— The dark matter density profiles of DG1 (left) and DG2 (right). The circles represent the dark matter density profiles derived from the dark matter rotation curves shown in Fig. 4. The short dashed and dash-dotted lines indicate the mass density profiles derived using the best fitted NFW and pseudo-isothermal halo models in Fig. 4, respectively. The open and filled rectangles indicate the density profiles of DG1LT and DG1DM, respectively. See Section 2 for more details. The inner slope of the profile is measured by a least squares fit (dotted lines) to the data points less than 1.0 kpc as indicated by gray dots. In the right panel the long dashed line indicates a least squares fit, excluding the innermost point. The measured inner slope α is shown in the panel. The true dark matter density profiles in the simulations are also overplotted as indicated by open stars. The vertical gray dotted lines indicate the force resolution (86 pc) of the simulations.

ermost measured radii are all less than $\sim$80 km s^{-1}, the CDM rotation curve with $V_{200}\sim$90 km s^{-1} (i.e., small dots in Fig. 6) can be regarded as a lower limit to the maximum rotation velocities of the galaxies.

As shown in the left panel of Fig. 6, the scaled rotation curves of the THINGS dwarf galaxies are similar to each other, showing a linear increase in the inner regions. The inner shapes of the rotation curves are better described by pseudo-isothermal halo models (dashed lines) than the NFW models. This implies that the THINGS dwarf galaxies have core-like dark matter distributions at their centers (see Oh et al. 2011 for more discussion). Similarly, the scaled rotation curves of DG1 and DG2 are consistent with those of the THINGS dwarf galaxies. They significantly deviate from the CDM rotation curves at the inner regions and, like the THINGS dwarf galaxies, they increase too slowly to match the steep rotation curves of the CDM halos.

4.3. *The dark matter density profile*

A more direct way to examine the central matter distributions in galaxies is to convert the galaxy rotation curve to the mass density profile. In particular, the measurement of the inner slope of the profile provides a stringent observational constraint on the "cusp/core" problem. With an assumption of a spherical mass distribution for the galaxy halo, the galaxy rotation curve $V(R)$ can be converted to the mass density profile $\rho(R)$ by the following formula (see de Blok et al. 2001 and Oh et al. 2008, 2011 for more details),

$$\rho(R) = \frac{1}{4\pi G}\left[2\frac{V}{R}\frac{\partial V}{\partial R} + \left(\frac{V}{R}\right)^2\right], \quad (4)$$

where V is the rotation velocity observed at radius R, and G is the gravitational constant. Here we do not decontract the halos since in these galaxies adiabatic contraction does not occur and rather expansion happens as shown in Governato et al. (2010) (see also Dutton et al. 2007).

Using Eq. 4, we derive the dark matter density profiles of the THINGS dwarf galaxies, DG1 and DG2 as well as the CDM halos whose rotation curves are shown in the left panel of Fig. 6. In addition, we also derive the corresponding mass density profiles of the best fitted pseudo-isothermal halo models to the THINGS dwarf galaxies. As shown in the right panel of Fig. 6, despite the scatter, both DG1 and DG2 have shallower mass density profiles than dark matter only simulations. Instead, they are more consistent with the THINGS dwarf galaxies showing near–constant density dark matter distributions at the centers.

In Fig. 7, we compare the derived dark matter density profiles of DG1 and DG2 with their true full 3−D dark matter density distribution. The inner decrease in the actual dark matter density profiles of Fig. 7 is due to the shape of the potential in the region below the force resolution (86 pc). As shown in Fig. 7, for DG1, the observationally derived dark matter density profile robustly traces the true values but that for DG2 it is found to be on average a factor of three lower than its true value at the central regions. This is mainly due to the lower gas

rotation velocity of DG2 as shown in panel (f) of Fig. 3, resulting in smaller velocity gradients $\partial V/\partial R$ in Eq. 4 and thus smaller densities. However, considering the uncertainties in deriving the profile, the recovered profile is acceptable to examine the central dark matter distribution.

We determine the inner density slopes α assuming a power law ($\rho \sim r^{\alpha}$) and find them to be α=-0.31 ± 0.07 for DG1 and α=-0.49 ± 0.06 for DG2, respectively. If we re-measure the slope of DG2, excluding the innermost point which has a large errorbar, the slope is flatter (α=-0.27 ± 0.05) as indicated by the long dashed line in the right panel of Fig. 7. These slopes deviate from the steep slope of $\sim$$-1.0$ from dark-matter-only cosmological simulations. The profiles of both DG1 and DG2 deviate from NFW models beyond about 10 times the force resolution. This tells us that the baryonic feedback processes in dwarf galaxies can affect the dark matter distribution in such a way that the central cusps predicted from dark-matter-only simulations are flattened, resulting in dark matter halos characterised by a core, as found in normal dwarf galaxies in the local universe.

5. CONCLUSIONS

In this paper, we have compared the dark matter distribution of the dwarf galaxies from a novel set of SPH+N-body simulations by Governato et al. (2010) with that of 7 THINGS dwarf galaxies to address the "cusp/core" problem in ΛCDM. The simulations were performed in a fully cosmological context, and include the effect of baryonic feedback processes, particularly strong gas outflows driven by SNe. Both the simulated and the observed dwarf galaxies have similar kinematic properties, and have been analyzed in a homogeneous and consistent manner as described in Oh et al. (2011). The techniques used in deriving dark matter density profiles were found to provide accurate results when compared with the true underlying profiles, supporting the veracity of the techniques employed by observers. Therefore, this provides a quantitative comparison between the simulations and the observations, and allows us to examine how the baryonic feedback processes affect the dark matter distribution at the centers of dwarf galaxies.

From this, we test the general predictions from ΛCDM simulations: (1) the steep rotation curve inherent in the central cusp, and (2) the steep inner slope of $\sim$$-1.0$ of the dark matter density profiles. We find that the dark matter rotation curves of the newly simulated dwarf galaxies rise less steeply at the centers than those from dark-matter-only simulations. Instead, they are more consistent with those of the THINGS dwarf galaxies. In addition, the mean value of the inner density slopes α of the simulated dwarf galaxies is $\simeq$$-0.4 \pm 0.1$. Compared to the steep slope of $\sim$$-1.0$ predicted from the previous dark-matter-only simulations (including our simulations run with DM only), these flat slopes are in better agreement with α=-0.29 ± 0.07 found in the 7 THINGS dwarf galaxies analysed by Oh et al. (2011).

In conclusion, the results described in this paper confirm that energy transfer and subsequent gas removal in a clumpy ISM have the net effect of causing the central DM distribution to expand, while at the same time limiting the amount of baryons at the galaxy center. By the present time the DM central profile in galaxies DG1 and DG2 is well approximated by a power law with slope α of $\sim$$-0.4 \pm 0.1$. These values of α are significantly flatter than in the collisionless control run and are in agreement with those of observed shallow DM profiles in nearby dwarf galaxies.

SHOH acknowledges financial support from the South African Square Kilometre Array Project. FG acknowledges support from HST GO-1125, NSF ITR grant PHY-0205413 (also supporting TQ), NSF grant AST-0607819 and NASA ATP NNX08AG84G. The work of WJGdB is based upon research supported by the South African Research Chairs Initiative of the Department of Science and Technology and National Research Foundation. We thank the computer resources and technical support by TERAGRID, ARSC, NAS and the UW computing center, where the simulations were run.

REFERENCES

Begeman, K. 1989, A&A, 223, 47
Bell, E. F. & de Jong, R. S. 2001, ApJ, 550, 212
Benson, A. J. & Madau, P. 2003, MNRAS, 344, 835
Blais-Ouellette, S., Carignan, C., Amram, P., & Côté, S. 1999, AJ, 118, 2123
Bolatto, A. D., Simon, J. D., Leroy, A., & Blitz, L. 2002, ApJ, 565, 238
Boylan-Kolchin, M., Springel, V., White, S. D. M., Jenkins, A., & Lemson, G. 2009, MNRAS, 398, 1150
Brooks, A. M., Governato, F., Booth, C. M., Willman, B., Gardner, J. P., Wadsley, J., Stinson, G., & Quinn, T. 2007, ApJ, 655, L17
Bruzual, G. & Charlot, S. 2003, MNRAS, 344, 1000
Bureau, M. & Carignan, C. 2002, AJ, 123, 1316
Ceverino, D. & Klypin, A. 2009, ApJ, 695, 292
Ciotti, L. & Ostriker, J. P. 2001, ApJ, 551, 131
Conroy, C. & Wechsler, R. H. 2009, ApJ, 696, 620
Dalcanton, J. J. & Stilp, A. M. 2010, ApJ, 721, 547
de Blok, W. J. G. & McGaugh, S. S. 1997, MNRAS, 290, 533
de Blok, W. J. G., McGaugh, S. S., Bosma, A., & Rubin, V. C. 2001, ApJ, 552, 23
de Blok, W. J. G., Walter, F., Brinks, E., Trachternach, C., Oh, S.-H., & Kennicutt, R. C. 2008, AJ, 136, 2648
De Lucia, G. & Blaizot, J. 2007, MNRAS, 375, 2
Diemand, J., Kuhlen, M., Madau, P., Zemp, M., Moore, B., & Potter, D. Stadel, J. 2008, Nature, 454, 735
Dutton, A. A. 2009, MNRAS, 396, 121
Dutton, A. A., van den Bosch, F. C., Dekel, A., & Courteau, S. 2007, ApJ, 654, 27
El-Zant, A., Shlosman, I., & Hoffman, Y. 2002, ApJ, 560, 636
Gentile, G., Burkert, A., Salucci, P., Klein, U., & Walter, F. 2005, AJ, 634, L145
Ghigna, S., Moore, B., Governato, F., Lake, G., Quinn, T., & Stadel, J. 2000, ApJ, 544, 616
Gnedin, N. Y. 2010, ApJ, 721, L79
Gnedin, O. Y. & Zhao, H. 2002, MNRAS, 333, 299
Governato, F., Brook, C., Mayer, L., Brooks, A., Rhee, G., Wadsley, J., Jonsson, P., Willman, B., Stinson, G., Quinn, T., & Madau, P. 2010, Nature, 463, 203
Governato, F., Brook, C. B., Brooks, A. M., Mayer, L., Willman, B., Jonsson, P., Stilp, A. M., Pope, L., Christensen, C., Wadsley, J., & Quinn, T. 2009, MNRAS, 398, 312
Governato, F., Willman, B., Mayer, L., Brooks, A., Stinson, G., Valenzuela, O., Wadsley, J., & Quinn, T. 2007, MNRAS, 374, 1479
Guo, Q., White, S. D. M., Li, C., & Boylan-Kolchin, M. 2010, MNRAS, 404, 1111
Haardt, F. & Madau, P. 1996, ApJ, 461, 20
Hayashi, E. & Navarro, J. F. 2006, MNRAS, 373, 1117
Jonsson, P., Groves, B. A., & Cox, T. J. 2010, MNRAS, 403, 17
Katz, N. & White, S. D. M. 1993, ApJ, 412, 455

Kennicutt, Jr., R. C., Armus, L., Bendo, G., Calzetti, D., Dale, D. A., Draine, B. T., Engelbracht, C. W., Gordon, K. D., Grauer, A. D., Helou, G., Hollenbach, D. J., Jarrett, T. H., Kewley, L. J., Leitherer, C., Li, A., Malhotra, S., Regan, M. W., Rieke, G. H., Rieke, M. J., Roussel, H., Smith, J., Thornley, M. D., & Walter, F. 2003, PASP, 115, 928
Klypin, A., Kravtsov, A. V., Bullok, J. S., & Primack, J. R. 2001, ApJ, 554, 903
Klypin, A., Kravtsov, A. V., Valenzuela, O., & Prada, F. 1999, ApJ, 522, 82
Larson, R. B. 1974, MNRAS, 169, 229
Li, C. & White, S. D. M. 2009, MNRAS, 398, 2177
Mashchenko, S., Couchman, H. M. P., & Wadsley, J. 2006, Nature, 442, 539
Mashchenko, S., Wadsley, J., & Couchman, H. M. P. 2008, Science, 319, 174
Mastropietro, C., Moore, B., Mayer, L., Wadsley, J., & Stadel, J. 2005, MNRAS, 363, 509
McGaugh, S. S., Barker, M. K., & de Blok, W. J. G. 2003, ApJ, 584, 566
McGaugh, S. S., Schombert, J. M., de Blok, W. J. G., & Zagursky, M. J. 2010, ApJ, 708, 14
Mo, H. J. & Mao, S. 2004, MNRAS, 353, 829
Moore, B. 1994, Nature, 370, 629
Moore, B., Ghigna, S., Governato, F., Lake, G., Quinn, T., Stadel, J., & Tozzi, P. 1999a, ApJ, 524, 19
Moore, B., Quinn, T., Governato, F., Stadel, J., & Lake, G. 1999b, MNRAS, 310, 1147
Moster, B. P., Somerville, R. S., Maulbetsch, C., van den Bosch, F. C., Macciò, A. V., Naab, T., & Oser, L. 2010, ApJ, 710, 903
Navarro, J. F., Frenk, C. S., & White, S. D. M. 1995, MNRAS, 275, 56
—. 1996, ApJ, 462, 563
—. 1997, ApJ, 490, 493
Navarro, J. F., Hayashi, E., Power, C., Jenkins, A. R., Frenk, C. S., White, S. D. M., Springel, V., Stadel, J., & Quinn, T. R. 2004, MNRAS, 349, 1039
Navarro, J. F., Ludlow, A., Springel, V., Wang, J., Vogelsberger, M., White, S. D. M., Jenkins, A., Frenk, C. S., & Helmi, A. 2010, MNRAS, 402, 21
Navarro, J. F. & Steinmetz, M. 2000, ApJ, 528, 607
Navarro, J. F. & White, S. D. M. 1994, MNRAS, 267, 401
Oh, S.-H., de Blok, W. J. G., Brinks, E., Walter, F., & Kennicutt, Jr, R. C. 2011, arXiv:1011.0899, AJ accepted
Oh, S.-H., de Blok, W. J. G., Walter, F., Brinks, E., & Kennicutt, R. C. 2008, AJ, 136, 2761
Okamoto, T., Gao, L., & Theuns, T. 2008, MNRAS, 390, 920
Power, C., Navarro, J. F., Jenkins, A. R., Frenk, C. S., White, S. D. M., Springel, V., Stadel, J., & Quinn, T. 2002, MNRAS, 338, 14
Quinn, T., Katz, N., & Efstathiou, G. 1996, MNRAS, 278, L49
Read, J. I. & Gilmore, G. 2005, MNRAS, 356, 107
Reed, D., Governato, F., Verde, L., Gardner, J., Quinn, T., Stadel, J. Merritt, D., & Lake, G. 2005, MNRAS, 357, 82
Rhee, G., Valenzuela, O., Klypin, A., Holtzman, J., & Moorthy, B. 2004, ApJ, 617, 1059
Robertson, B. E. & Kravtsov, A. V. 2008, ApJ, 680, 1083
Sánchez-Janssen, R., Méndez-Abreu, J., & Aguerri, J. A. L. 2010, MNRAS, 406, L65
Simon, J. D., Bolatto, A. D., Leroy, A., & Blitz, L. 2003, ApJ, 596, 957
Simon, J. D. & Geha, M. 2007, ApJ, 670, 313
Spekkens, K., Giovanelli, R., & Haynes, M. P. 2005, AJ, 129, 2119
Springel, V., Wang, J., Vogelsberger, M., Ludlow, A., Jenkins, A., Helmi, A., Navarro, J. F., Frenk, C. S., & White, S. D. M. 2008, MNRAS, 391, 1685
Springel, V., White, S. D. M., Jenkins, A., Frenk, C. S., Yoshida, N., Gao, L., Navarro, J., Thacker, R., Croton, D., Helly, J., Peacock, J. A., Cole, S., Thomas, P., Couchman, H., Evrard, A., Colberg, J., & Pearce, F. 2005, Nature, 435, 629
Stadel, J., Potter, D., Moore, B., Diemand, J., Madau, P., Zemp, M., Kuhlen, M., & Quilis, V. 2009, MNRAS, 398, L21
Stanimirović, S., Staveley-Smith, L., & Jones, P. A. 2004, ApJ, 604, 176
Stark, D. V., McGaugh, S. S., & Swaters, R. A. 2009, AJ, 139, 312
Stinson, G., Seth, A., Katz, N., Wadsley, J., Governato, F., & Quinn, T. 2006, MNRAS, 373, 1074
Stoehr, F., White, S. D. M., Springel, V., Tormen, G., & Yoshida, N. 2003, MNRAS, 345, 1313
Suyu, S. H., Marshall, P. J., Auger, M. W., Hilbert, S., Blandford, R. D., Koopmans, L. V. E., Fassnacht, C. D., & Treu, T. 2010, ApJ, 711, 201
Swaters, R. A., Madore, B. F., van den Bosch, F. C., & Balcells, M. 2003, ApJ, 583, 732
Tonini, C., Lapi, A., & Salucci, P. 2006, ApJ, 649, 591
Trujillo-Gomez, S., Klypin, A., Primack, J., & Romanowsky, A. J. 2010, ArXiv e-prints
Valenzuela, O., Rhee, G., Klypin, A., Governato, F., Stinson, G., Quinn, T., & Wadsley, J. 2007, ApJ, 657, 773
van den Bosch, F. C., Burkert, A., & Swaters, R. A. 2001, MNRAS, 326, 1205
van den Bosch, F. C., Robertson, B. E., Dalcanton, J. J., & de Blok, W. J. G. 2000, AJ, 119, 1579
van der Marel, R. P. & Franx, M. 1993, ApJ, 407, 525
Verde, L., Peiris, H. V., Spergel, D. N., Nolta, M. R., Bennett, C. L., Halpern, M., Hinshaw, G., Jarosik, N., Kogut, A., Limon, M., Meyer, S. S., Page, L., Tucker, G. S., Wollack, E., & Wright, E. L. 2003, ApJS, 148, 195
Wadsley, J. W., Stadel, J., & Quinn, T. 2004, New A, 9, 137
Walter, F., Brinks, E., de Blok, W. J. G., Bigiel, F., Kennicutt, R. C., Thornley, M., & Leroy, A. 2008, AJ, 136, 2563
White, S. D. M. & Rees, M. J. 1978, MNRAS, 183, 341